Eur. Phys. J. E (2015) **38**: 40
DOI 10.1140/epje/i2015-15040-5

THE EUROPEAN PHYSICAL JOURNAL E

Regular Article

Numerical simulation of subaqueous chute flows of granular materials

C. Varsakelis[a] and M.V. Papalexandris

Institute of Mechanics, Materials and Civil Engineering, Université catholique de Louvain, B1348 Louvain-la-Neuve, Belgium

Received 12 January 2015 and Received in final form 16 March 2015
Published online: 21 May 2015 –

Abstract. In this paper we report on numerical studies of unsteady, gravity-driven flow of a subaqueous erodible granular bed on an inclined plane. According to our simulations, the evolution of the flow can be partitioned in three phases. In the first phase, due to the onset of an interfacial instability, the material interface deforms into a series of long waves. In the second phase, these waves are transformed to skewed vortex ripples that grow in time and eventually coalesce. The computed wavelengths of these ripples are in good agreement with previously reported experimental measurements. In the third phase of the flow evolution, the high fluid velocities wash out the vortex ripples and a layer of rapidly moving particles is formed at the material interface. The predicted granular velocities comprise two segments: a concave one at the vicinity of the material interface, where the maximum is attained, followed by a slightly convex one, where they decrease monotonically to zero. The same trend has been reported in experimental results for the corresponding steady flows. Finally, we investigate via a parametric study the effect of the configuration stresses, which represent contact forces between grains. As it turns out, such stresses have a stabilizing effect, in the sense that increasing their magnitude inhibits the formation of vortex ripples.

1 Introduction

Subaqueous debris flows and avalanches, sediment transport and pyroclastic density currents are typical examples of geophysical processes that involve gravity-driven flows of particulate solids immersed in fluids. The occurrence of such natural phenomena is usually associated with significant adverse effects. Consequently, advancing our understanding and predictive capacity of these flows is important for the mitigation of the threats that they pose. It is, therefore, not surprising that intense research efforts have been devoted to their study, resulting in a large body of scientific literature.

Such geophysical processes are typically of very large scale and, as such, are difficult to reproduce in the laboratory or in numerical simulations. For this reason, the majority of research studies typically focuses on small-scale flows which constitute idealized and simplified prototypes but can still provide important information for the original geophysical processes as well. As regards experimental studies, three different configurations have been investigated: rotating drums and circulatory and non-circulatory flumes. For example, Courech du Pont *et al.* [1], systematically measured the duration and amplitude of granular avalanches in rotating drums, for various densities, particle sizes and fluid viscosities. They additionally determined the scales of the flow based on the density ratio and the Stokes number, *i.e.* the ratio of grain inertia to fluid viscosity. The pertinence of the Stokes number has also been confirmed by Armanini *et al.* [2] who conducted experiments on steady flows of PVC pellets immersed in water. On the other hand, by investigating the steady flow of steel beads immersed in three different fluids (air, water and a glycerine-water mixture), Jain *et al.* [3] reported the existence of striking similarities between the velocity profiles emerging in dry and in fluid-saturated granular flows. Subsequently, the important results of Jain *et al.* [3] have been corroborated by other experimental studies; see, for example, Cassar *et al.* [4], Doppler *et al.* [5] and references therein.

Alongside experimental studies, research efforts have also been devoted to the numerical investigation of fluid-saturated granular flows in the presence of gravity. To this extent, emphasis has been placed on sediment transport (both viscous and turbulent) and, in particular, on the mechanisms that drive the erosion of sediment beds, the migration and transport of particles and the formation of patterns (*e.g.* dunes and ripples). As regards studies that investigated numerically either turbulent or viscous sediment transport in correlation with the ratio of the phasial densities, we refer the reader to Durán *et al.* [6,7], Schmeeckle [8] and Páhtz *et al.* [9]. On the other hand, as regards the properties of aeolian particle transport, we refer to the numerical studies of Carneiro *et al.* [10], Carneiro *et al.* [11], Durán *et al.* [12] and references therein.

[a] e-mail: christos.varsakelis@uclouvain.be

All the aforementioned studies employ a Discrete Element Method (DEM) for the modelling of the granular phase (solid particles) coupled with the Navier-Stokes equations for the fluids, appropriately augmented to account for the interactions between the two phases in the form of momentum exchange. An alternative approach to modelling fluid-saturated granular flows is offered by continuum two-phase models. According to these models, both the fluid and the granular material are treated as generalized continua; see, for example, Drew and Passman [13] for a detailed exposition as well as next section. This approach is advantageous in the dense regime, especially when the number of particles (per unit area and globally) becomes disproportionably large.

However, numerical simulations of the flows of interest based on two-phase models are quite scarce and remain a challenging task to perform. The dearth of numerical results can be attributed mainly to the size and complexity of these models. In fact, two-phase models contain balance equations for each phase. Therefore, the resulting number of governing equations is significantly higher than the ones for single-phase flows such as, for example, the Navier-Stokes equations for simple fluids. Further, these models contain expressions for the interactions between the two phases in the form of momentum and energy exchange. Typically, these expressions consist of nonlinear differential and relaxation terms which increase significantly the complexity of the equations in hand. Moreover, the mathematical models have a multitude of length and time scales associated with them; this is due to the fact that fluid-saturated granular materials have a complex micro-structure and do not exhibit scale segregation. It should also not go unnoticed that these models incorporate several physical parameters whose values are not always known precisely.

As a result of the above, the majority of available numerical results for gravity-driven flows of fluid-saturated granular materials, based on continuum two-phase models, correspond to steady-state, one-dimensional flows, [14–16]. However, it is well known that the flows of interest have a rich phenomenology and are susceptible to both long- and short-wave hydrodynamic instabilities. Evidently, such phenomena cannot be captured by the steady-state approximation. Instead, one has to consider unsteady and multi-dimensional flows.

In this paper, we investigate the unsteady gravity-driven flow of a subaqueous erodible granular bed, down an inclined plane, via direct numerical simulations. We consider large angles of inclination, namely $a \geq 30°$, so as to ensure the triggering of hydrodynamic instabilities. Our study is based on the mixture theory for fluid-saturated granular materials previously developed in Papalexandris [17]. The numerical treatment of the mathematical model is performed via an algorithm for two-phase continua, recently proposed in Varsakelis and Papalexandris [18]. This is a projection-type numerical method, suitably generalized for two-velocity–two-pressure models, that is able to treat strong material interfaces associated with steep gradients of particle concentration.

The objective of the present study is twofold. First, to systematically study the properties of the flows of interest and gain physical insight on the mechanisms that drive their evolution. In this respect, emphasis is placed on the deformation of the material interface between the granular bed and the interstitial fluid lying above it. The secondary objective of this study is to assess the predictive capacity of the model in hand for the flows of interest. For this reason, the numerically predicted flow quantities are compared against experimental measurements, whenever the latter are available and to the extent that such a comparison is feasible.

2 Mathematical model and numerical method

We consider an isotropic granular material, saturated by a simple fluid, that occupies a domain Ω. Both phases are assumed to have constant density. Further, we postulate that dilatancy effects are negligible so that the motion of the granular material can be approximated by that of an incompressible, fluid-like body; for more information concerning this assumption and its validity the reader is referred to Málek and Rajagopal [19].

Papalexandris [17] proposed a two-phase flow model for fluid-saturated granular materials based on the mixture-theory approach. According to this formalism, the mixture is treated as the union of two open subsystems that are allowed to interact with each other in the form of momentum and energy exchanges. Each phase is endowed with its own set of state variables and velocity vector and it is required to satisfy the equations for the balance of mass, linear momentum and energy, separately.

In the continuum theory of Papalexandris [17], for the description of the state of the granular phase, the volume fraction and its spatial gradient are introduced as additional thermodynamic variables. The rationale for augmenting the state vector of the granular phase by including these particular variables goes back to Goodman and Cowin [20]. It is based on the observation that the available "useful" work that can be extracted from the granular conglomerate is restricted by the configuration of the grains in space. The adequate description of the grain-configuration, in turn, is a geometric problem and in the continuum level requires a measure for i) the volume that the granular material occupies (volume fraction) and ii) the intergranular area density (volume fraction gradient). Based on these arguments, Goodman and Cowin [20] postulated that the Helmholtz free energy of the granular material should explicitly depend on the volume fraction and its spatial gradient which is equivalent to including these quantities as additional thermodynamic variables related to the miscrostructure of the granular material. Although the theory of Goodman and Cowin [20] was devised for dry granular flows, it has subsequently been extended to fluid-saturated ones by Passman *et al.* [21], Wang and Hutter [22], Massoudi and Mehrabadi [23], Papalexandris [17] and others.

Once the state space of the granular and the fluid phase have been fixed, constitutive expressions for the

various terms that describe dissipative phenomena (*e.g.* viscosity coefficients, interphasial drag, etc.) are derived by exploiting the constrains imposed by the second thermodynamic axiom concerning the non-negativity of the entropy production rate. Further, this procedure straightforwardly yields a rate equation for the volume fraction usually referred to as the compaction equation. Importantly, as demonstrated by Baer and Nunziato [24], the absence of such equation leads to underdeterminacy issues. Also, due to the inclusion of the volume-fraction gradient as a thermodynamic variable, an additional non-dissipative component of the granular material's stress tensor emerges, the so-called configuration tensor, which involves the volume-fraction gradients associated in a non-Newtonian way. The properties of this tensor are discussed in detailed below.

The derivation of continuum models for either dry or fluid-saturated granular flows invokes the continuum hypothesis. For the mixtures of interest, due to the microstructure of granular materials, this hypothesis asserts that the validity of continuum models breaks down in length scales smaller than or equal to the grain diameter. At such length scales, the employment of hybrid models that couple a DEM for the solid particles with a continuum description for the fluid phase is deemed better adapted.

The mathematical model of Papalexandris [17] can be seen as the two-phase analogue of the Navier-Stokes-Fourier equations that additionally takes into account the non-Newtonian character of the granular materials. Its incompressible limit was systematically derived by Varsakelis and Papalexandris [25], upon generalization of low-Mach-number asymptotics to multiphase flows. Under the additional assumption of no-dilatancy, the non-dimensional governing equations read:

Mass and momentum balance equations for the granular phase:

$$\nabla \cdot \boldsymbol{u}_s = 0, \tag{1}$$

$$\begin{aligned}\rho_s \phi_s \frac{\mathrm{d}\boldsymbol{u}_s}{\mathrm{d}\, t_s} + \nabla(\phi_s p_s) = \frac{1}{Re}\nabla \cdot (\mu_s \phi_s \boldsymbol{S}_s) \\ -\nabla \cdot (\Gamma_s \nabla\phi_s \otimes \nabla\phi_s) \\ +p_f \nabla\phi_s + \delta\,(\boldsymbol{u}_f - \boldsymbol{u}_s) \\ +\rho_s \phi_s \boldsymbol{g}.\end{aligned} \tag{2}$$

Mass and momentum balance equations for the fluid phase:

$$\nabla \cdot ((\boldsymbol{u}_s - \boldsymbol{u}_f)\phi_f) = 0, \tag{3}$$

$$\begin{aligned}\rho_f \phi_f \frac{\mathrm{d}\boldsymbol{u}_f}{\mathrm{d}\, t_f} + \nabla(\phi_f p_f) = \frac{1}{Re}\nabla \cdot (\mu_f \phi_f \boldsymbol{S}_f) \\ -(p_f \nabla\phi_s + \delta\,(\boldsymbol{u}_f - \boldsymbol{u}_s)) \\ +\rho_f \phi_f \boldsymbol{g}.\end{aligned} \tag{4}$$

Compaction equation:

$$\frac{\mathrm{d}\phi_s}{\mathrm{d}t_s} = 0. \tag{5}$$

Here, the subscripts "s" and "f" denote the granular and fluid phase, respectively. Further, ρ_i, ϕ_i and $\boldsymbol{u}_i = (u_{i_1}, u_{i_2}, u_{i_3})$, $i = s, f$ are the density, volume fraction and velocity vector of the phase i. Also, p_s and p_f are the "dynamic" pressures of the granular and fluid phase, respectively; they are completely equivalent to the pressure term that appears in the Navier-Stokes equations. Additionally, μ_i is the viscosity coefficient of the phase i and $\boldsymbol{g}$ is the gravity vector.

The operators $\frac{\mathrm{d}}{\mathrm{d}\, t_i} = \frac{\partial}{\partial t} + \boldsymbol{u}_i \cdot \nabla$ and $\boldsymbol{S}_i$ stand for the material derivative and the traceless deviatoric part of the deformation tensor of phase i, $i = s, f$, respectively. The above governing equations are closed by the saturation condition

$$\phi_s + \phi_f = 1. \tag{6}$$

The momentum exchange between the two phases is represented by the combined term $p_f \nabla\phi_s + \delta(\boldsymbol{u}_f - \boldsymbol{u}_s)$, appearing on the right-hand side of the momentum equations (2) and (4), albeit with opposite sign. More specifically, the term $\delta(\boldsymbol{u}_f - \boldsymbol{u}_s)$ models the interphasial drag exerted on the solid particles by the fluid, with δ being a term proportional to the interphasial drag coefficient. Further, the non-conservative product $p_f \nabla\phi_s$ models nozzling effects and its presence is dictated by thermodynamic considerations. Its presence follows from the constitutive assumption that the volume fraction ϕ_s is carried by the granular phase; in particular, as asserted by Bdzil *et al.* [26], discarding such terms leads to mathematical models that violate the second thermodynamic axiom.

The viscosity of the granular phase μ_s describes the rheology of the granular material. As such, it is not constant but can generally depend, among others, on the particle concentration ϕ_s, the strain rate $\dot{\gamma}_{ij}$, the normal stress p_s and others. Therefore, the choice of the rheology can lead to vastly different profiles for the variables of the two phases. We will elaborate further on the choice of the rheology in due course.

The term $\Gamma_s \nabla\phi_s \otimes \nabla\phi_s$, whose divergence enters the momentum equation of the granular phase (2), is the *configuration stress tensor*, mentioned above, and, accordingly, Γ_s is the *configuration stress coefficient*. The presence of the configuration stress tensor asserts that the model in hand i) allows for density (volume fraction) gradients at equilibrium, ii) predicts that the granular material supports non-zero shear stresses at equilibrium, iii) predicts that, at equilibrium, the normal and shear stresses are connected via a Coulomb-Mohr stress-strain relation that links the angle of internal friction to ϕ_s and $\nabla\phi_s$.

2.1 Numerical method

The numerical methodology employed for the integration of the governing equations is described in detail in the recent article of Varsakelis and Papalexandris [18].

Therefore, only an outline of it is presented herein. The algorithm constitutes a generalization of projection-type methods, on collocated grids, to multi-phase flows and employs a predictor-corrector scheme for the integration in time. The generalized flux-interpolation method proposed in Lessani and Papalexandris [27,28] is employed for the integration of the convective terms to remedy the well-known odd-even decoupling phenomenon that occurs in collocated grids. Additionally, stiffness problems due to steep volume-fraction gradients in the vicinity of material interfaces are treated via a regularization method.

Schematically, the flow-chart of the algorithm reads:

i) The values of the volume fraction, ϕ_s are computed by integrating the compaction equation (5) via the multi-dimensional upwind scheme of Colella [29].

ii) The algorithm searches for interfaces by checking the magnitude of $\nabla\phi_s$. In the vicinity of the interface, the predicted values of ϕ_s are replaced by those of smoother, compactly supported function obtained via a parabolic regularization of the compaction equation.

iii) A projection method is employed for the computation of the granular pressure p_s and velocity $\boldsymbol{u}_s$. In particular, the pressure p_s is computed via solving numerically a Poisson equation. Once p_s has been computed, $\boldsymbol{u}_s$ is calculated via the standard Helmholtz decomposition.

iv) In our case, $\boldsymbol{u}_f$ is not divergence free; see eq. (3), which requires a generalization of the standard projection method. This results in a second order elliptic PDE with variable coefficients for the pressure p_f. Once p_f is computed, then $\boldsymbol{u}_f$ is calculated via the Helmholtz-Marsden decomposition.

3 Numerical results

We study numerically the response of an erodible granular bed of constant thickness, placed on an inclined plane, to the combined effect of gravity and the shearing by an interstitial fluid. We remark that the physical parameters that we are using are given in dimensional form. For clarity purposes, all dimensional variables are denoted with a hat symbol, "ˆ".

3.1 Mixture parameters and computational set-up

We consider a mixture of water with coarse sand. The sand is assumed to be monodisperse and its diameter $\hat{d}_p$ is taken equal to 1 mm. The densities of water and sand are $\hat{\rho}_f = 1000\,\mathrm{kg/m^3}$ and $\hat{\rho}_s = 2200\,\mathrm{kg/m^3}$, respectively.

As regards the configuration stress coefficient Γ_s, we assume the following expression:

$$\hat{\Gamma}_s = \hat{k}_2 \hat{\rho}_s \phi_s. \tag{7}$$

Here, $\hat{k}_2$ is a (strictly positive) material-dependent constant. As such, its value should be obtained experimentally. However, and to the best of our knowledge, systematic experimental measurements for $\hat{k}_2$ have yet to appear in the literature. On the other hand, Varsakelis and Papalexandris [30] estimated numerically the value of $\hat{k}_2$ by computing the equilibrium distributions of granular materials and the forces acting on them. On the basis of this study, we first choose herein $\hat{k}_2 = 4 \times 10^{-5}\ \mathrm{m^4/s^2}$. Later on this work we assess the effect of modifying its value.

For the rheology of the granular material we proceed as follows. Our starting point is a Krieger-Dougherty-type law for the effective normal and shear viscosity of suspensions, acquired experimentally by Boyer *et al.* [31], that reads

$$\eta^{\mathrm{shear}} = 1 + 2.5\phi_s \left(1 - \frac{\phi_s}{\phi_c}\right)^{-1} + \mu^c \frac{\phi_s}{(\phi_c - \phi_s)^2}\,, \tag{8}$$

$$\eta^{\mathrm{normal}} = \frac{\phi_s}{(\phi_c - \phi_s)^2}\,. \tag{9}$$

Here, η^{shear} and η^{normal} designate the apparent shear and normal viscosity of the suspension, respectively whereas ϕ_c represents the maximum packing fraction. Further, μ^c is given by the following relation:

$$\mu^c = \mu_1 + \frac{(\mu_2 - \mu_1)}{1 + I_0 \phi_s^2 (\phi_c - \phi_s)^{-2}}\,. \tag{10}$$

In the above relation, μ_1, μ_2 and I_0 are experimentally determined constants. As $\phi_s \to \phi_c$ the suspension approaches the jamming transition and both the shear and normal viscosity diverge to infinity at a rate of $O((\phi_c - \phi_s)^{-2})$. For dilute mixtures, the shear viscosity approaches Einstein's law $(1 + 2.5\phi_s)$ at a rate of $O(\phi_s)$. Importantly, eqs. (8) and (9) constitute the volume-fraction representation of the so-called $\mu(I)$-rheology for suspensions of particles in fluids.

For the accommodation of (8) to the governing equations we assume that the contribution of the fluid phase to the viscous stress tensor of the mixture is negligibly small. In other words, the shear and normal viscosity of the granular phase are only related to (8) and (9), correspondingly. Further, since the model at hand concerns isochoric motions for the granular material, the stress tensor of the granular phase does not have a component that models the bulk viscous pressure, *i.e.* it is traceless. Consequently, only the shear viscosity $\hat{\eta}^{\mathrm{shear}}$ is needed in our case. In order to derive the relation that links η^{shear} to $\hat{\mu}_s$, we first recall that

$$\hat{\boldsymbol{\tau}}_s = \eta^{\mathrm{shear}} \hat{\mu}_f \phi_s \hat{\dot{\boldsymbol{\gamma}}}_s, \tag{11}$$

$$\phi_s \hat{\boldsymbol{\tau}}_s = \hat{\mu}_s \phi_s \hat{\dot{\boldsymbol{\gamma}}}_s, \tag{12}$$

where $\hat{\boldsymbol{\tau}}_s$ is the viscous stress tensor. The multiplication by ϕ_s on the right-hand sides of the above equations is needed in order to recover the correct single-phase limits as $\phi_s \to 0, 1$, Drew and Passman [13]. Then, the combination of (11) and (12) with (8) yields

$$\hat{\mu}_s = \eta^{\mathrm{shear}} \hat{\mu}_f. \tag{13}$$

As documented in various studies, *e.g.*, Stickel and Powell [32], the classical Krieger-Dougherty relation, *i.e.*

the third term of equation (8), is sufficient to recover Einstein's formula for the rheology of dilute suspensions. The proof of this argument is a direct consequence of the binomial theorem. Based on this fact, in our simulations we have set

$$\hat{\mu}_s = \hat{\mu}_f \mu^c \frac{\phi_s}{(\phi_c - \phi_s)^2}\,, \tag{14}$$

and following Savage [33], Passman *et al.* [34] and Wang and Hutter [15], we have set $\hat{\mu}_f \mu^c = 727\,\mathrm{kg}/(\mathrm{m}\cdot\mathrm{s})$.

Still, the rheology law given by (14) has a singularity at $\phi_s = \phi_c$ which numerically is extremely cumbersome to compute. For the circumvention of this issue, we introduce an *ad hoc* finite, upper bound for η^{shear} and, more specifically, we employ $\phi_c = 1$. This regularization bypasses the difficulties associated with the singularity but comes at a price; the correct angle of repose cannot be captured by the numerical simulations. In other words, the governing equations predict that the mixture will always be set in motion for every angle of inclination. In other words, in this context, equilibrium is identified with a creeping motion.

On the other hand, the interstitial fluid, water, is assumed to be a simple Newtonian fluid at constant temperature. As such, its dynamic viscosity is taken to be constant and equal to $\hat{\mu}_f = 1 \times 10^{-3}\,\mathrm{kg}/(\mathrm{m}\cdot\mathrm{s})$.

As regards the interphasial drag coefficient $\hat{\delta}$, the force density exerted by the fluid on the particles is approximated by the drag on a sphere moving at constant speed at low Reynolds numbers. This results in the following expression for $\hat{\delta}$:

$$\hat{\delta} = \phi_s\, 18\, \frac{\hat{\mu}_f}{\hat{d}_p^2}\, Q(Re_p). \tag{15}$$

For the function $Q(Re_p)$, the empirical relationship of Rowe [35] is used

$$Q(Re_p) = \begin{cases} 1 + 0.15\, Re_p^{0.687}, & Re_p < 1000, \\ 0.01833\, Re_p, & Re_p \geq 1000, \end{cases} \tag{16}$$

where Re_p is the particle Reynolds number, defined with respect to the relative grain velocity, *i.e.*,

$$Re_p = \frac{\hat{\rho}_f\, \hat{d}_p}{\hat{\mu}_f} |\hat{\boldsymbol{u}}_s - \hat{\boldsymbol{u}}_f|. \tag{17}$$

In our study, all physical parameters are non-dimensionalized as follows. The phasial densities and pressures have been non-dimensionalized with respect to the density of water, $\hat{\rho}_{\mathrm{ref}} = 1000\,\mathrm{kg}/\mathrm{m}^3$, and atmospheric pressure, $p_{\mathrm{ref}} = 10^5\,\mathrm{Pa}$, respectively. Also, the initial thickness of the granular layer, $\hat{h}$, and the reference velocity $u_{\mathrm{ref}} = \sqrt{\hat{g}\,\hat{h}}$ have been used for the non-dimensionalization of lengths and velocities, respectively. Further, the viscosity coefficients have been non-dimensionalized with respect to the viscosity of the mixture $\mu_{\mathrm{ref}} = (\rho_s \phi_{s,\mathrm{in}} \mu_s + \rho_f \phi_{f,\mathrm{in}} \mu_f)/(\rho_s \phi_{s,\mathrm{in}} + \rho_f \phi_{f,\mathrm{in}})$, where $\phi_{s,\mathrm{in}}$ stands for the initial distribution of particles. For the problem in hand, $\mu_{\mathrm{ref}} \equiv 608\,\mathrm{kg}/(\mathrm{m}\cdot\mathrm{s})$ and, accordingly, the Reynolds number of the flow is equal to approximately 0.2. For comparison purposes, it is worth noting that if we had used the fluid viscosity as reference, $\mu_{\mathrm{ref}} = \mu_f$, then the Reynolds number would have been equal to 210.

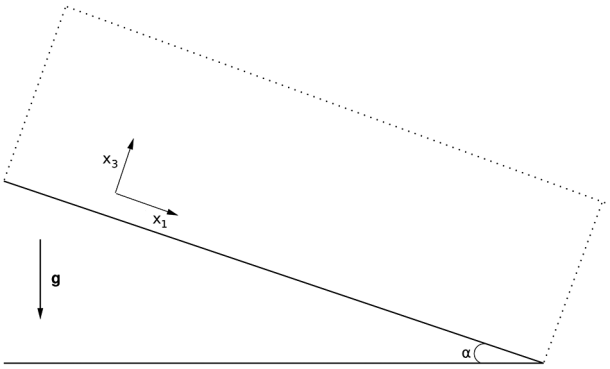

Fig. 1. Configuration of the numerical experiments.

In our numerical experiments, the mixture is placed on the surface of a plane inclined at an angle a to the streamwise direction, as shown in fig. 1. A Cartesian coordinate system is employed with x_1 the streamwise and x_3 the normal direction. The dimensions of the computational domain are $l = 20$ and 4 in the streamwise and normal directions, respectively. An equidistant mesh of 500×100 cells is used to discretize the computational domain. Finally, we set $\Delta t = 0.005\ \Delta x_3$.

As regards boundary conditions, the flow is assumed to be periodic in the streamwise (x_1) direction, with period equal to l. At the bottom of the computational domain, which coincides with the inclined plane, the no-slip condition is prescribed for the phasial velocities and zero-Neumann conditions are prescribed for both the phasial pressures and the volume fraction. On the other hand, the top boundary of the computational domain is considerably far from the material interface. For this reason, at this boundary, the free-slip boundary condition is applied for the phasial velocities whereas zero-Neumann conditions are assigned to the phasial pressures and the volume fraction.

For the initial condition of the particle concentration, we consider a dense ($\phi_s = 0.7$) granular layer of constant thickness $h = 1$, placed on the inclined plane. This profile is superimposed to a sinusoidal perturbation of period l and amplitude $h/5$, so as to trigger the erosion of the material interface. Outside the granular bed, the domain is filled with water. As regards the initial conditions for the other variables, we assume that the entire mixture is at rest so that the flow is induced by gravity.

3.2 Reference case: a = 30°

For the reference case, the angle of inclination is set to $a = 30°$. According to the experimental measurements of Cassar *et al.* [4], for such an angle of inclination and

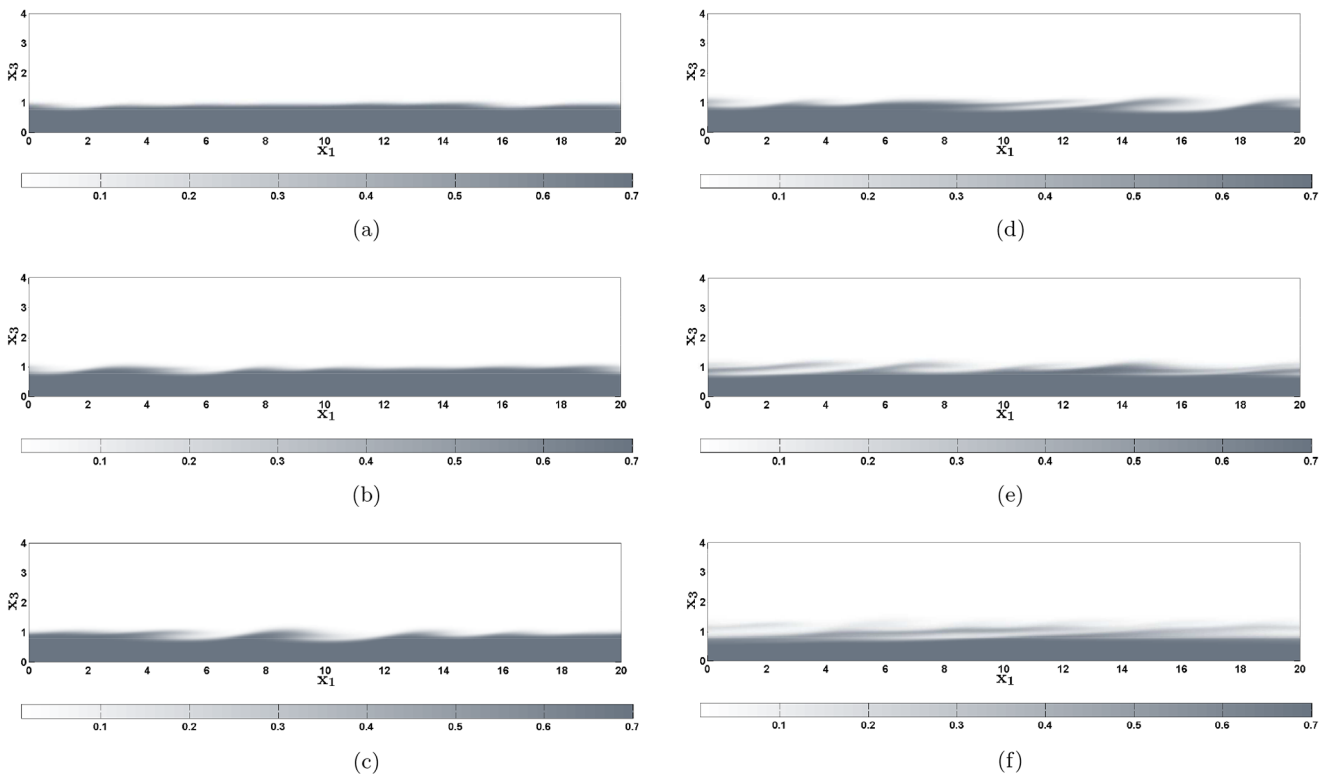

Fig. 2. Iso-contours of particle concentration ϕ_s. (a) $t = 24.5$, (b) $t = 30$, (c) $t = 37$, (d) $t = 43$, (e) $t = 49$, (f) $t = 73$. The material interface deforms into a series of long waves which are transformed into skewed, vortex ripples that grow in time and also coalesce. Eventually, the fluid velocity becomes large enough in the neighborhood of the interface and the ripples are washed out.

with the mixture parameters that have been employed, the flow is not expected to reach a steady state. As will be shown below, this has been observed in our simulations as well.

We begin the discussion of the numerical results with the evolution of the material interface. Figures 2(a)-(f) show the particle concentration at various time instances. The evolution of the flow can be partitioned in three distinct phases. During the first phase, which lasts until approximately $t \simeq 36.7$, the material interface deforms into a series of wavy patterns due to the onset of an interfacial instability. The wavelengths of these patterns are large, accounting for approximately 1/4 of the length of the computational domain; this is in agreement with previous studies on two-layer flows of both Newtonian and non-Newtonian fluids down inclined planes; see, for example, Millet *et al.* [37] and references therein. Moreover, these long waves are reminiscent to the ones reported in Cassar *et al.* [4]; see also the earlier study of Prasad *et al.* [38].

The second phase of the flow, which starts at $t \simeq 36.7$ and lasts until $t \simeq 62$, is characterized by the transformation of the density waves to skewed almost triangular patterns. The height of these patterns spans a few decades of grain diameters. Accordingly, these patterns are referred to as *ripples* (in large-scale flows, such as the ones encountered in sediment transport, these patterns are commonly referred to as *dunes*). The wavelengths of the ripples increase with time and eventually the ripples coalesce. The formation, propagation and coalescence of ripples at the material interface is a typical feature of the flows of interest and has been confirmed experimentally in a variety of configurations; see, for example, the recent review article of Charru *et al.* [39].

To date, the exact mechanism of ripple formation is not fully understood. As noted, among others, in Sleath [40], there is some consensus that their origin is due to hydrodynamic instabilities and, more specifically, due to the fact that the inertia of the interstitial fluid plays a destabilizing role in the shearing of an erodible bed. Charru and Hinch [41,42] have asserted this point of view via a linear stability analysis for both steady and unsteady flows, and have determined the stabilizing role of crest erosion as a function of the Galileo number. In turn, if the formation of ripples is engendered by the interaction between the two phases, this implies that an adequate description of the flows of interest requires the consideration of the dynamics of both phases; a consequence that is in agreement with the results of Meruane *et al.* [43]. More recently, Durán *et al.* [12], who investigated the formation of aeolian ripples via direct numerical simulations, proposed a different mechanism. According to these authors, the dominant mechanism of formation involves resonant grain trajectories, of suitable lengths, and the subsequent reptation. In other words, in the view of Durán *et al.* [12], the formation of aeolian ripples is non-hydrodynamic.

For the case under study, the Galileo number is quite large

$$Ga = \frac{(\hat{\rho}_s - \hat{\rho}_f)}{\hat{\rho}_f} \frac{\hat{\rho}_f^2 \hat{d}_p^2}{\hat{\mu}_f^2} \approx 10^4.$$

For such values of the Galileo number, the analysis of Charru and Hinch [41,42] predicts the formation of ripples, due to hydrodynamic instabilities. On the other hand, we have $\hat{\rho}_f/\hat{\rho}_s = 1/2.2$ and $\hat{\mu}_f = 10^{-3}\,\mathrm{kg}/(\mathrm{m}\cdot\mathrm{s})$. These values are quite different from those employed in Durán *et al.* [12] so that extrapolating their conclusions to problem at hand needs a judicious investigation of different interstitial fluids, which goes beyond the scopes of the present study.

As can be inferred from figs. 2(c) and (d), the crests of the predicted ripples are oriented downstream. This is in agreement with the experimental observations of Doppler *et al.* [44] and Loiseleux *et al.* [45] which assert that the orientation of the crests always follows the direction of the motion of the interstitial fluid. Interestingly, in both these studies, the interstitial fluid is forced to flow upwards the inclined plane. Still, the orientation of the crests of the ripples follows the direction of the fluid motion.

At $t \simeq 61.2$ the vortex ripples begin to wash out. This marks the beginning of the third phase of evolution which lasts until the termination of the simulation at $t = 100$. During this phase, the ripples are eventually damped and they are replaced by a shear layer of rapidly moving particles. The damping of the vortex ripples is attributed to the high streamwise velocity of the interstitial fluid, which accelerates continuously due to gravity. In fact, the phenomenon of damping of vortex ripples, generated at low velocities, at high velocities is well known; see, for example, Van Rijn [46].

Alternatively, one could seek a correlation between the damping of the ripples and the values of the Shields number of the flow, θ, defined as follows:

$$\theta = \frac{\tau}{(\rho_s - \rho_f) g d_p}\,, \tag{18}$$

where τ stands for the shear stresses exerted on the material interface while the denominator is the apparent weight of a grain. Upon comparison of previous experimental studies, Nielsen [47] concluded that the formation of vortex ripples is possible only if $\theta < 1$. By contrast, for $\theta > 1$, the ripples are washed out and the motion resembles that of a sheet flow, *i.e.* the particles move as a granular sheet whose thickness can range from a few to several decades of grain diameters; see, for example, the analysis presented in Wilson [48]. In our case, however, the Shields number of the flow remains at the order of 10^{-1}. In turn, this implies that the damping of the predicted vortex ripples is solely attributed to the high fluid velocities in the neighborhood of the interface.

Next, we turn our attention to the granular velocity profiles. First, it is important to remark that, to the best of our knowledge, experimental measurements of the instantaneous velocity profiles for the flows of interest are not available in the literature. For this reason, we have opted to juxtapose our numerical predictions against experimental evidence acquired from steady flows at lower inclination angles and discuss differences and notable similarities.

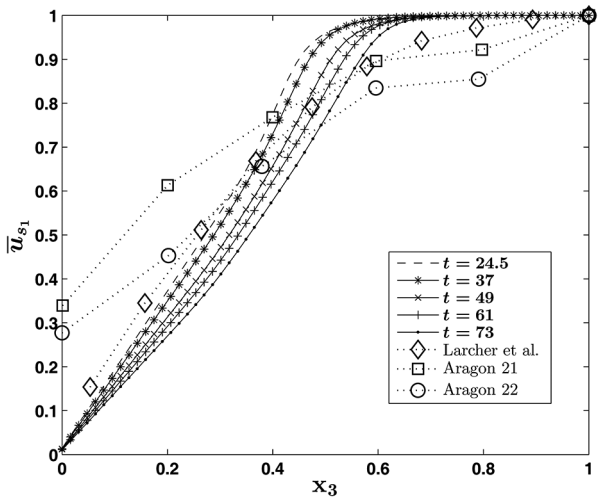

Fig. 3. Predicted granular velocity profiles $\overline{u}_{s_1}$ plotted against depth at various times juxtaposed to the experimental measurements of Larcher *et al.* [36] and Aragon [14]. In the first stages of the flow, the predicted profiles are in good agreement with those of Larcher *et al.* [36]. As the flow evolves, quantitative comparison becomes less favorable but the qualitative trend remains similar.

Let $\overline{u}_{s_1}$ denote the normalized, streamwise-averaged, granular velocity component, in the streamwise direction. Figure 3 shows plots of $\overline{u}_{s_1}$, against depth x_3, at different time instances. In the same figure we have also plotted the experimental measurements of Larcher *et al.* [36] and of Aragon [14], normalized accordingly. The velocities attain their maximum value at the material interface whereas away from it they decrease rapidly. This decrease consists roughly of two segments: a concave one at the vicinity of the material interface and a slightly convex one below. This trend is shared by the experimental measurements of Larcher *et al.* [36], which are also quantitatively similar to the numerical predictions at the first stages of the flow. As the flow evolves, and hydrodynamic instabilities manifest, the quantitative agreement becomes less accurate; still, the qualitative trend remains similar. Discrepancies are more evident when comparison is attempted against the profiles of Aragon [14]. Interestingly, the experimental measurements of Aragon [14] illustrate the existence of a considerable slip at the lower plane, so that the two segments of different curvature are not easily distinguishable. We may note that since the no-slip condition has been employed for both phases such slip phenomena cannot be captured by our numerical simulations.

Further insight to the flow properties can be obtained upon examination of the vorticity field of the fluid. Figures 4(a)-(c) depict iso-contours of the magnitude of the fluid phase vorticity field at times $t = 30$, 43 and 73, respectively. We observe that the shearing of the granular

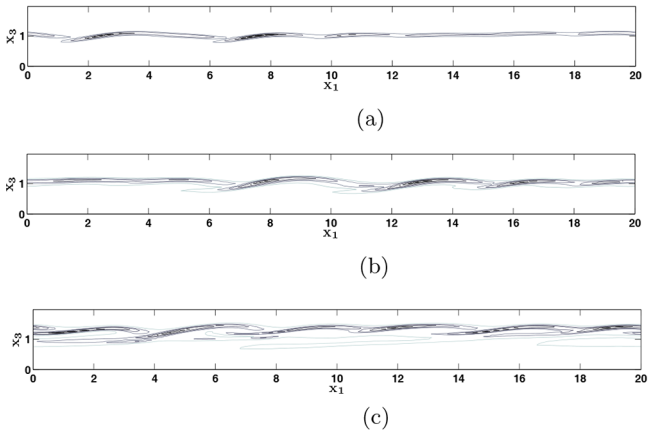

Fig. 4. Iso-contours of the vorticity field of the fluid phase at (a) $t = 30.6$, (b) $t = 43$, (c) $t = 73$. Vortical structures are observed over the material interface. At $t = 43$, when the ripples have been formed, lee vortices are formed downstream the crest of each ripple.

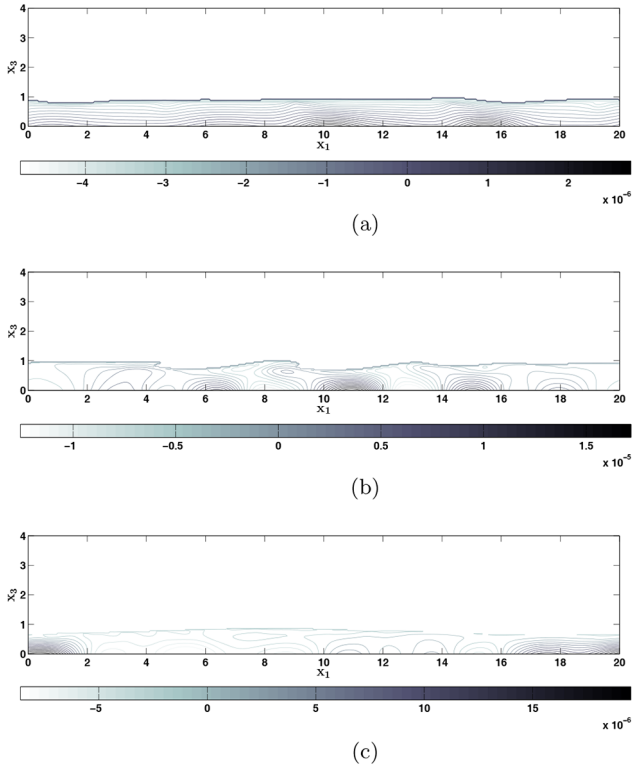

Fig. 5. Iso-contours of the difference of the phasial pressures Δp at times (a) $t = 30$, (b) $t = 43$, (c) $t = 73$. The pressures are maintained at different levels for all times due to the interphasial drag and the configuration stresses. However, the amplitude of their difference remains at the order of 10^{-4}.

medium by the interstitial fluid results in the formation of vortices that are shed from the material interface. The height of these vortices is approximately ten times smaller than their length in the streamwise direction. Moreover, as the flow evolves, they are subject to streamwise stretching. Upon comparison of figs. 2(c) and (d) with figs. 4(b) and (c), we infer that the observed vortices are located

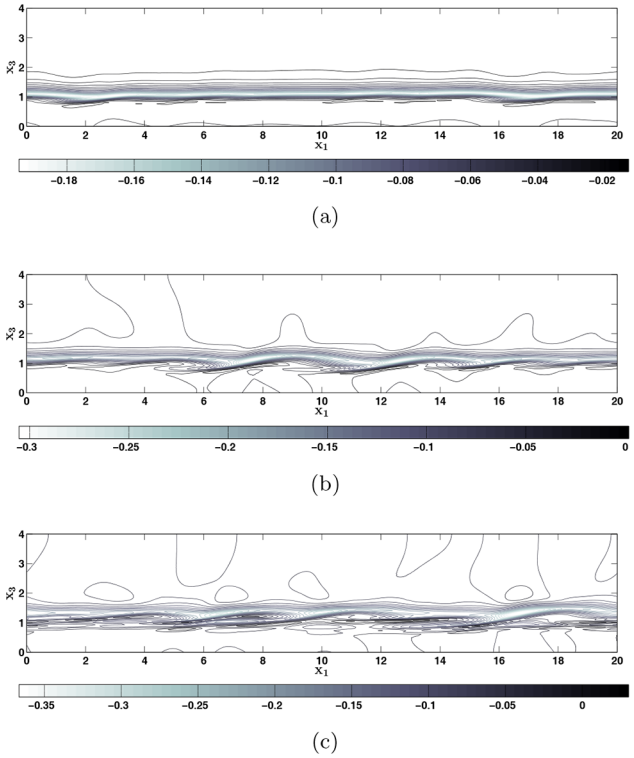

Fig. 6. Iso-contours of the difference of the phasial velocities Δu at times (a) $t = 30$, (b) $t = 43$, (c) $t = 73$. The two phases respond differently to gravitational forces. In fact, due to the density and viscosity bias, the fluid moves faster than the solid particles. Still, the difference is small and remains at the order of 10^{-1}.

downstream each ripple's crest. Therefore, in accordance with Bagnold's classical terminology, we deduce that these ripples are actually *vortex* ripples.

Wang and Hutter [15] studied numerically the steady flow of a water-sand mixture, down an inclined plane, and reported that both the phasial pressures and the velocities are maintained at different levels. In view of these results, it is interesting to examine whether the two phases eventually reach mechanical equilibrium. To this end, in figs. 5(a)-(c) and figs. 6(a)-(c) we have plotted the evolution of the differences of the phasial pressures $\Delta p = (p_s - p_f)$ and velocities $\Delta u = u_{s,1} - u_{f,1}$, respectively. It can be readily inferred that the mixture remains out of mechanical equilibrium throughout the duration of the simulation. Moreover, the negative sign of Δu in most areas of the domain shows that the fluid accelerates faster than solid particles do; this is due to the density and viscosity bias between the two phases. Still, the magnitudes of Δp and Δu are relatively small, at the order of 10^{-4} and 10^{-1}, respectively.

Figures 7(a)-(c) show iso-contours of the configuration stresses at $t = 43$. From these figures, we deduce that both the normal and the shear configuration stresses are maximized in the neighborhood of the material interface, where steep volume-fraction gradients are confined. On the other hand, away from this interface, they approach

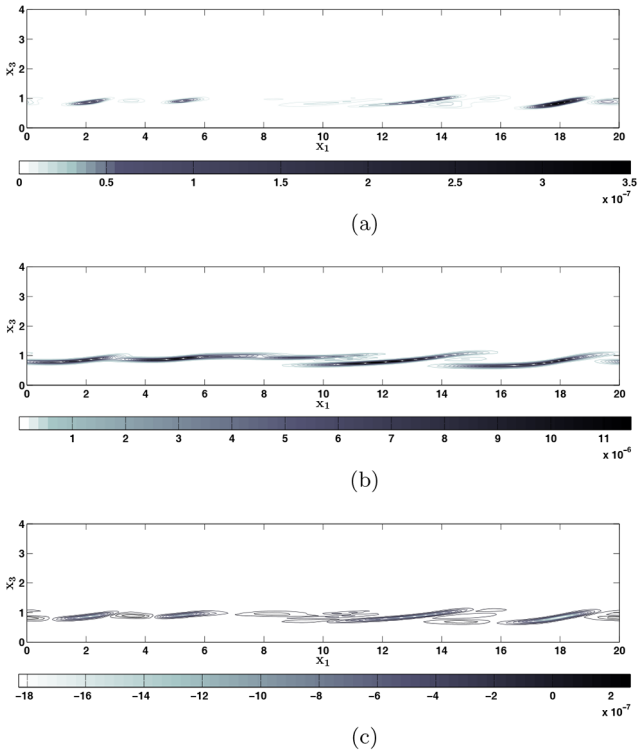

Fig. 7. Iso-contours of the configuration stresses at $t = 43$. (a) σ_{11}, (b) σ_{22}, (c) σ_{12}. Both the normal and the shear configuration stresses are maximized in the vicinity of the material interface, where the volume-fraction gradients are larger. Away from this area, the configuration stresses decay rapidly to zero.

rapidly zero. This result indicates that at the vicinity of the material interface, $\nabla(p_s - p_f)$ is counterbalanced by the combined effect of the configuration stresses and the interphasial drag, $\delta(u_s - u_f)$. By contrast, in the bulk of granular layer, where the particle concentration is constant, $\nabla(p_s - p_f)$ is solely offset by the interphasial drag.

Finally, for this reference case, a grid-convergence study has also been performed in order to validate the grid-independence of the numerical results. To this end, we have calculated and compared the mesh-dependent L^1-norm of the error for the phasial pressures p_s, p_f, the phasial velocities $\boldsymbol{u}_s$, $\boldsymbol{u}_f$ and the volume fraction ϕ_s. As usual, the mesh-dependent L^1 norm of the error is defined as

$$\mathrm{Err}(F) = \frac{1}{N}\sum_{i=1}^{N} |f_i - F_i|. \tag{19}$$

In the above equation, N stands for the number of computational cells whereas f_i and F_i are the numerical prediction and the exact solution evaluated at the cell i, respectively. In our study, the following grid sizes have been considered: 250×50, 500×100, 1000×200 and 2000×400. In the absence of an analytic solution, F has been chosen as the numerical prediction obtained with the finest grid of the study, namely, 4000×800 points. Figures 8(a) and (b) show the results of the grid-convergence study for the variables $\boldsymbol{u}_s$, $\boldsymbol{u}_f$ and ϕ_s, respectively, juxtaposed to

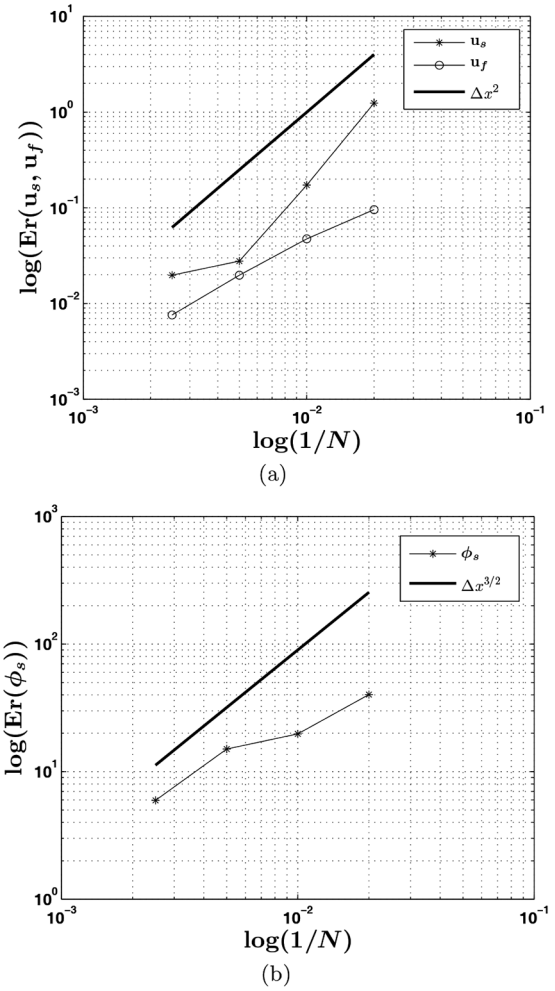

Fig. 8. Grid-convergence study. (a) $\boldsymbol{u}_s$, $\boldsymbol{u}_f$, (b) ϕ_s.

an estimate of the convergence rate. It can be evidenced that numerical convergence is achieved with refinement of the grid.

3.3 On the wavelengths of the vortex ripples

As mentioned above, the formation of vortex ripples is a typical feature of the flows of interest. For this reason, various studies have been devoted to the study of their properties. In particular, emphasis has been placed on the evaluation of their wavelengths via both experimental measurements and linear stability analyses. However, as commented in Charru *et al.* [49], the experimentally measured wavelengths exhibit large scatter which makes the assessment of numerical and theoretical predictions difficult.

Despite this conundrum, empirical correlations for the wavelengths of the ripples have already appeared in the literature. Herein, we compare the predicted wavelengths against the correlations of Coleman and Melville [50], and Coleman and Eling [51], derived from experiments on water-sand and air-sand mixtures. Both correlations

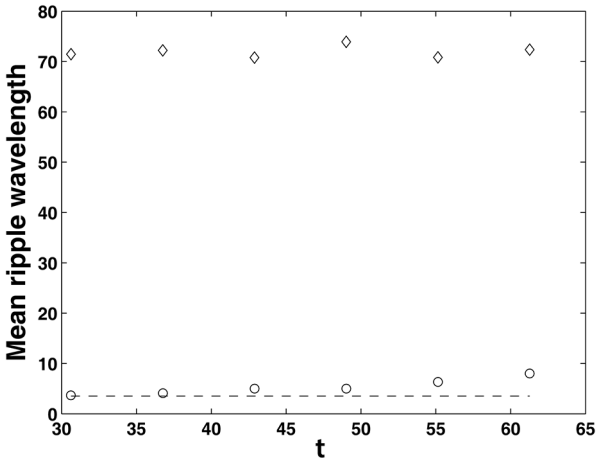

Fig. 9. Comparison of the predicted mean ripple wavelengths (○) and the ones obtained from the empirical correlations of Coleman and Melville [50] (♢), and Coleman and Eling [51] (−−). In our study, the numerically predicted wavelengths are in good agreement with the correlation of Coleman and Eling [51].

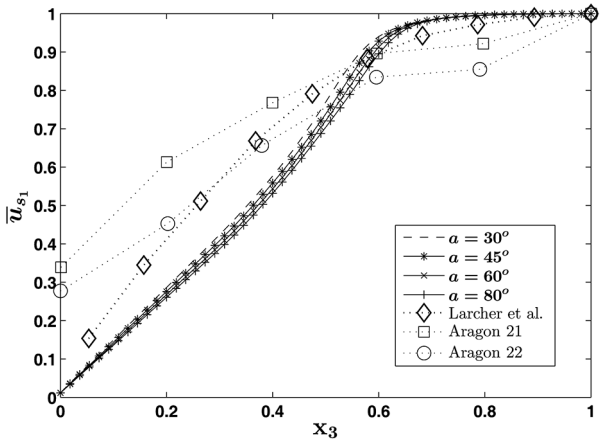

Fig. 10. Predicted granular velocity profiles $\overline{u}_{s_1}$ plotted against depth for various angles of inclination juxtaposed to the experimental measurements of Larcher *et al.* [36] and Aragon [14]. The qualitative trend remains unchanged for all angles of inclination. However, discrepancies become larger as the inclination angle increases.

associate the wavelength of the ripple with the particle diameter and read, respectively,

$$\frac{\lambda}{d_p} = 10^{2.5}\, Re_{pt}^{-0.2}, \tag{20}$$

$$\frac{\lambda}{d_p} = 175\, d_p^{0.75}. \tag{21}$$

Here, λ is the wavelength of the ripple whereas $Re_{pt} = \hat{u}^* \hat{d}_p \hat{\rho}_f / \hat{\mu}_f$ is the particle Reynolds number defined with respect to the friction velocity of the fluid at the surface of the granular layer, $\hat{u}^*$.

Figure 9 shows the numerically computed mean wavelength of the ripples at various instances of the flow *vis-à-vis* the values calculated from (20) and (21). It can be readily inferred that the predicted wavelengths are in good agreement with the values acquired from the correlation of Coleman and Eling, (21), throughout the duration of the simulation. On the other hand, the correlation of Coleman and Melville, (20), predicts wavelengths that are higher by an order of magnitude than the ones predicted herein, for all time instances. For the sake of completeness, we mention that we have compared the predicted mean-ripple wavelengths, obtained from simulations with different d_p, to the ones given by (20) and (21). Again, the predicted wavelengths are in good agreement with the ones computed by (21).

4 Parametric studies: angle of inclination and configuration stress coefficient

In order to study the sensitivity of the predicted features of the flow to changes in physical parameters we have conducted two parametric studies. More specifically, we have assessed the effects of modifying i) the angle of inclination a and, ii) the magnitude of the constant k_2 while maintaining the remaining parameters and the computational set-up identical to the reference case. The results from these studies are summarized below.

4.1 Angle of inclination

Modifying the angle of inclination amounts to changing the force that drives the flow. Since in the present study our focus is on unsteady granular flows, we have considered angles of inclination larger than the one employed in the reference case. In particular, we have used angles between 30° and 80°. Our simulations predict, as before, three phases of evolution of the material interface. Moreover, the characteristics of these phases of evolution are the same as in the reference case. In particular, the emergence of surface density waves and the formation, propagation, coalescence and damping of vortex ripples, are evidenced for all angles of inclination. Still, as the angle of inclination increases, the duration of the first two phases of the evolution becomes shorter because the growth of the streamwise phasial velocity components increases with the angle of inclination.

In view of the above, it is interesting to compare the granular velocity profiles at different angles of inclination. Figure 10 depicts profiles of $\overline{u}_{s_1}$, plotted against depth, for $a = 30°$, 45°, 60° and 80°. In this figure we have also superimposed the experimental measurements of Larcher *et al.* [36] and Aragon [14]. Similarly to the reference case, the numerical predictions are in better agreement with the experimental measurements of Larcher *et al.* [36]. However, it can be readily inferred that, although the qualitative trend remains roughly unchanged, the discrepancies increase with the angle of inclination. In other words, as

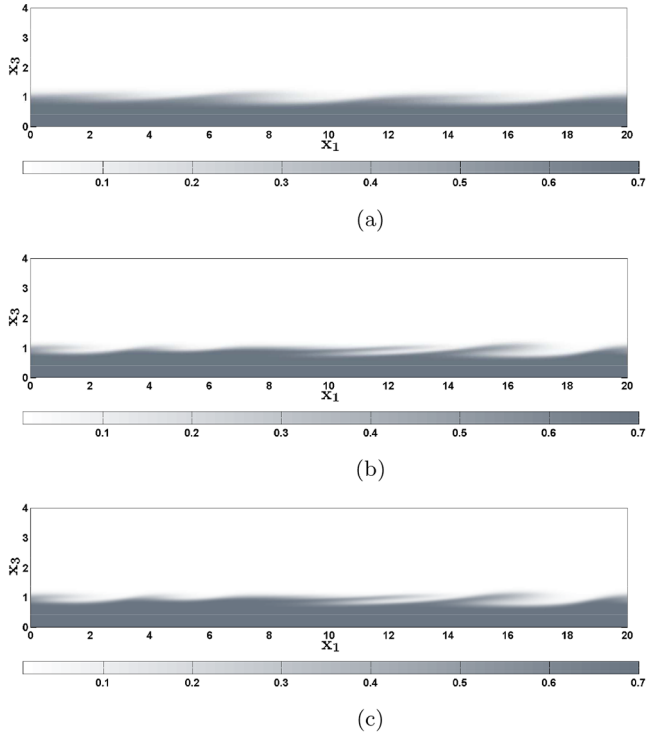

Fig. 11. Iso-contours of the particle concentration ϕ_s for various values of k_2 at $t = 43$. The increase of k_2 renders the relative motion of grains more difficult. For $k_1 > 10^{-2}$, the strength of the configuration stresses inhibits the formation of the ripples. In other words, the configuration stresses have a stabilizing effect and offset the inertia instability that is manifested during the second phase of the flow.

the inclination angle increases and the flow moves further away from the steady-state regime, the steady-state profiles become inadequate for the description of the flow properties.

4.2 Configuration stress coefficient

The configuration stress tensor $\Gamma\nabla\phi_s \otimes \nabla\phi_s$ has been introduced to model contact forces that are developed between the grains due to rearrangements in the distribution of the interfacial area density. By virtue of (7), as k_2 increases so do the configuration stresses. In turn, this renders the relative motions between the grains more difficult. Despite the fact that the configuration stress tensor appears in many models for granular materials, its influence on the flows of interest remains largely unexplored. For this reason, we present results of a parametric study with respect to the magnitude of the configuration stress coefficient k_2. The range of values of k_2 that we have considered is between 10^{-7} and 10^{-1}.

According to our simulations, for as long as $k_2 < 10^{-2}$, all features of the flow remain practically unchanged. However, for larger values of k_2, the evolution of the material interface changes considerably; this can be inferred from figs. 11(a)-(c) which depict the particle concentration for various values of k_2. More specifically, for $k_2 > 10^{-2}$, the patterns observed at the material interface are characterized by very low particle concentrations. In this respect, they are more reminiscent of rolling grains as opposed to vortex ripples. Rolling grains are transient patterns of low concentration formed at a material interface of a sheared, erodible bed; see, for example, Charru *et al.* [39]. Further, as demonstrated by Stegner and Wesfreld [52], rolling grains often gradually transform to ripples. However, in our case, this transition is not evidenced. In other words, the increasing magnitude of the configuration stresses inhibits the formation of vortex ripples.

As mentioned above, a key mechanism in the formation of the vortex ripples is the destabilization of the shearing of the material interface by the interstitial fluid's inertia. Therefore, our simulations suggest that, for larger values of k_2, the destabilizing role of the fluid's inertia is partially offset by the increased resistance of the particular phase to individual grain motions. In summary, we may conclude that the configuration stresses have a stabilizing effect to the flows of interest; this, to the best of our knowledge, has not been reported before.

5 Conclusions

In this paper, the unsteady gravity-driven flow of a subaqueous erodible granular bed on an inclined plane has been investigated via direct numerical simulations. Our simulations show that the evolution of the flow can be divided into three distinct phases. The first phase is characterized by the deformation of the material interface into a series of long waves. In the second phase the density waves transform into skewed vortex ripples. As the flow evolves, the ripples grow and eventually coalesce. The computed wavelengths of the ripples are in good agreement with available experimental data. In the third phase, the high fluid velocities wash out these ripples and a layer of rapidly moving particles forms at the material interface.

According to our numerical predictions, the instantaneous granular velocities attain their maximum value at the material interface whereas away from it they decrease rapidly to zero. The profiles of these velocities consist of two segments: a concave one, located in the vicinity of the material interface, and a slightly convex one, which extends until the surface of the inclined plane. Comparisons against previously acquired experimental results that correspond to steady flows yield two results. The qualitative trend is similar independently of the angle of inclination and the time that the instantaneous profiles are extracted. Second, quantitative agreement becomes less favorable as the flow evolves and as the inclination angle increases. We can, therefore, conclude that, even though the examination of the steady flows provides important information for the unsteady regime as well, it is not sufficient for the identification of all flow properties.

Finally, we have investigated the effect of the configuration stresses to the flow properties via a parametric study. These are contact forces that are developed between the grains and do not vanish even in the absence

of shear rates. The results of this parametric study indicate that the configuration stresses have a stabilizing effect to the flows of interest. More specifically, increasing their magnitude inhibits the formation of vortex ripples at the material interface.

The authors would like to thank the anonymous referee whose comments have improved the quality of the manuscript. Financial support for the first author has been provided by the National Research Fund of Belgium (FNRS) under the GRANMIX Projet de Recherche grant.

References

1. S. Courrech du Pont, P. Gondret, B. Perrin, M. Rabaud, Phys. Rev. Lett. **90**, 044301 (2003).
2. A. Armanini, H. Capart, L. Fraccarollo, M. Larcher, J. Fluid Mech. **532**, 269 (2004).
3. N. Jain, J.M. Ottino, R.M. Lueptow, J. Fluid Mech. **508**, 23 (2004).
4. C. Cassar, M. Nicolas, O. Pouliquen, Phys. Fluids **17**, 103301 (2005).
5. D. Doppler, P. Gondret, T. Loiseleux, S. Meyer, M. Rabaud, J. Fluid Mech. **577**, 161 (2007).
6. O. Durán, B. Andreotti, P. Claudin, Phys. Fluids **24**, 103306 (2012).
7. O. Durán, B. Andreotti, P. Claudin, Adv. Geosci. **37**, 73 (2014).
8. M. Schmeeckle, J. Geophys. Res. F **119**, 1240 (2014).
9. T. Pähtz, O. Durán, T.D. Ho, A. Valance, J. Kok, Phys. Fluids **27**, 013303 (2015).
10. M. Carneiro, T. Pähtz, H.J. Herrman, Phys. Rev. Lett. **107**, 098001 (2011).
11. M. Carneiro, N. Araújo, T. Pähtz, H.J. Herrman, Phys. Rev. Lett. **111**, 058001 (2013).
12. O. Durán, P. Claudin, B. Andreotti, Proc. Natl. Acad. Sci. U.S.A. **114**, 15665 (2014).
13. A.D. Drew, S.L. Passman, *Theory of Multicomponent Fluids* (Springer, 1999).
14. G. Aragon, J. Hydraul. Eng. **121**, 355 (1995).
15. Y. Wang, K. Hutter, Rheol. Acta **38**, 214 (1999).
16. B. Armanini, M. Larcher, E. Nucci, M. Dumbser, Adv. Water Resour. **63**, 1 (2014).
17. M.V. Papalexandris, J. Fluid Mech. **517**, 103 (2004).
18. C. Varsakelis, M.V. Papalexandris, J. Comput. Phys. **257**, 737 (2014).
19. J. Málek, K. Rajagopal, Mech. Mater. **38**, 233 (2006).
20. M.A. Goodman, S.C. Cowin, Arch. Rat. Mech. Anal. **44**, 249 (1972).
21. S.L. Passman, J.W. Nunziato, P.B. Bailey, J. Rheol. **20**, 167 (1986).
22. Y. Wang, K. Hutter, Granular Matter **73**, 163 (1999).
23. M. Massoudi, M.M. Mehrabadi, Acta Mech. **152**, 121 (2001).
24. M.R. Baer, J.W. Nunziato, Intl. J. Multiphase Flow **12**, 861 (1986).
25. C. Varsakelis, M.V. Papalexandris, J. Fluid Mech. **669**, 472 (2011).
26. J.B. Bdzil, R. Menikoff, S.F. Son, A.K. Kapila, D.S. Stewart, Phys. Fluids **11**, 378 (1999).
27. B. Lessani, M.V. Papalexandris, J. Comput. Phys. **212**, 218 (2006).
28. B. Lessani, M.V. Papalexandris, Int. J. Numer. Meth. Heat Fluid Flow **18**, 545 (2008).
29. P. Colella, J. Comput. Phys. **87**, 171 (1990).
30. C. Varsakelis, M.V. Papalexandris, J. Comput. Phys. **229**, 4183 (2010).
31. F. Boyer, E. Guazzelli, O. Pouliquen, Phys. Rev. Lett. **107**, 188301 (2011).
32. J.J. Stickel, R.L. Powel, Annu. Rev. Fluid Mech. **37**, 129 (2005).
33. S.B. Savage, J. Fluid Mech. **92**, 53 (1979).
34. S.L. Passman, J.P.J. Thomas, P.B. Bailey, J.W. Thomas, J. Eng. Mech. Div., A.S.C.E. **39**, 885 (1980).
35. P.N. Rowe, Trans. Int. Chem. Engng **48**, 175 (1961).
36. M. Larcher, L. Fraccarollo, A. Armanini, H. Capart, J. Hydraul. Res. **45**, 59 (2007).
37. S. Millet, V. Botton, H. Ben Hadid, D. Henry, F. Rousset, Phys. Rev. E **88**, 043004 (2013).
38. S.N. Prasad, D. Pal, M.J.M. Romkens, J. Fluid Mech. **413**, 89 (2000).
39. F. Charru, B. Andreotti, P. Claudin, Annu. Rev. Fluid Mech. **45**, 469 (2013).
40. J.F.A. Sleath, J. Hydraul. Res. **14**, 69 (1976).
41. F. Charru, E.J. Hinch, J. Fluid Mech. **550**, 111 (2006).
42. F. Charru, E.J. Hinch, J. Fluid Mech. **550**, 123 (2006).
43. C. Meruane, A. Tamburrino, O. Roche, J. Fluid Mech. **648**, 381 (2010).
44. D. Doppler, T. Loiseleux, P. Gondret, M. Rabaud, *Incipient grain transport and pattern formation at a sand surface sheared by a continuous laminar flow. Part II: large bed slope*, in *Proceedings of of the 2nd International Workshop on Marine Sandwave and River Dune Dynamics* (University of Twente, Enschede, 2004).
45. T. Loiseleux, P. Gondret, M. Rabaud, D. Doppler, Phys. Fluids **17**, 103304 (2003).
46. L.C.V. Rijn, *Principles of Sediment Transport in Rivers, Estuaries and Coastal Seas* (Aqua Publications, 1993).
47. P. Nielsen, J. Geophys. Res. **86**, 6467 (1981).
48. K.C. Wilson, J. Hydraul. Eng. **113**, 97 (1987).
49. F. Charru, Phys. Fluids **18**, 121508 (2007).
50. S. Coleman, B. Melville, J. Hydraul. Eng. **122**, 301 (1996).
51. S. Coleman, B. Eling, J. Hydraul. Res. **38**, 331 (2000).
52. A. Stegner, J.E. Wesfreld, Phys. Rev. E **60**, 3487 (1999).